# Suppressing DFB Lasers Relaxation Oscillations by High-Order Continuous Shaping Current With CNN Prediction

Qing-An Ding, Huixin-Liu, Xudong Cheng, Xiao-Juan Wang, Weiping Huang, *Senior Member, IEEE*, Liuge Du, Gaoyang Zhu, *Member, IEEE*, Li Zheng, and Qunying Yang

***Abstract*— A technique of continuous shaping current waveform to suppress relaxation oscillations (ROs) of distributed feedback (DFB) laser for a high-performance optic system is demonstrated. To effectively suppress ROs, expressions for the shaping current waveform are theoretically derived based on the rate equations and different polynomials for the 3rd, 5th, and 8th order Fourier basis functions are introduced. The convolutional neural network (CNN) is employed to predict the multi-parameter values that determine the results of the shaping input current, which exempt from the difficult and time-consuming process of parameter selection. Prior to training, preprocessing of the data obtained from DFB laser forward simulation using min-max normalization aims to improve the training efficiency of the CNN. The shaping current signals obtained from the CNN predicted parameters are put into the equivalent circuit model for the DFB laser to verify the effectiveness of the shaping current technique and CNN parameter optimization. Afterwards, the shaping current waveform is verified in a time division multiplex passive optical network (TDM-PON) utilizing the DFB laser model as a directly modulated source achieving remarkable performance with low cost. The results show that the high-order continuous shaping current modulated technique can successfully suppress the ROs and enhance the performance of the optic system.**

Manuscript received 28 September 2022; revised 28 January 2023 and 7 March 2023; accepted 8 March 2023. Date of publication 15 March 2023; date of current version 28 March 2023. This work was supported in part by the Shandong Natural Science Foundation, China, under Grant ZR2017MF070, Grant ZR2020MF014, and Grant ZR2021QF132; in part by the National Natural Science Foundation of China under Grant 61471224 and Grant 61801267; in part by the Scientific Research Foundation of Shandong University of Science and Technology for Recruited Talents under Grant skr-D-0104060540915. *(Corresponding authors: Liuge Du; Gaoyang Zhu.)*

Qing-An Ding is with the School of Electronics and Information Engineering and the Microwave and Optical Communication Studio, Shandong University of Science and Technology, Qingdao 266510, China.

Huixin-Liu, Xudong Cheng, Xiao-Juan Wang, Li Zheng, and Qunying Yang are with the Microwave and Optical Communication Studio and the College of Electronic Information Engineering, Shandong University of Science and Technology, Qingdao 266510, China.

Weiping Huang was with the Department of Electrical and Computer Engineering, McMaster University, Hamilton, ON L8S 4L8, Canada. He is now with the School of Information Science and Engineering, Shandong University, Qingdao 266237, China.

Liuge Du is with the School of Information Science and Engineering, Shandong University, Qingdao 266237, China (e-mail: lgdu@sdu.edu.cn).

Gaoyang Zhu is with the School of Electronics and Information Engineering, Shandong University of Science and Technology, Qingdao 266510, China (e-mail: gaoyangzhu@sdust.edu.cn).

Color versions of one or more figures in this article are available at https://doi.org/10.1109/JQE.2023.3257289.

Digital Object Identifier 10.1109/JQE.2023.3257289

***Index Terms*— DFB laser, continuous shaping current, convolutional neural network, TDM-PON.**

## I. INTRODUCTION

THE frequency selectivity of Bragg grating unique to distributed feedback (DFB) laser makes it one of the most effective methods for single longitudinal mode work at present [1]. DFB lasers are attractive optical sources for application in wavelength division multiplexing passive optical network (WDM-PON) [2], orthogonal frequency division multiplexing (OFDM) [3], and time division multiplexing (TDM) PON [4] with dynamic single longitudinal mode, narrow linewidth output, and good wavelength stability [5]. Therefore, an optical source with a smaller size, better quality, higher efficiency, and longer life for optical communication transmission systems has been researched for years to meet the increasing communication speed and capacity.

The DFB laser typically transmits optical communication information using either indirect or direct modulation. Indirect modulation, also known as external modulation, means that the laser is modulated by external equipment [6]. This technique is relatively mature but high-cost. Compared with external modulation, direct modulation has the advantages of simple structure and the cost is cheap [7], [8]. The disadvantage of direct modulation is that the output waveform will produce relaxation oscillations (ROs). Such ROs would cause serious distortion of the output waveform and limit the rate of optical communication systems [9]. In order to break through the limit of direct modulation, numerous techniques for suppressing ROs have been suggested including light injection [10], connecting an external electrical circuit to the laser diode [11], and appropriately shaping the modulated current waveform [12], etc.

Lucas Illing demonstrated a shaping current technique that appropriately shapes the driving current of DFB lasers to control the nonlinear internal degrees and optimize the optical intensity [13]. For the purpose of obtaining the relationship between photon density and modulation current, Hoang Nam researched the rate equations for semiconductor laser in a direct modulation mode [14]. Our research team has proposed an improved equivalent circuit model for DFB lasers considering the effects of parasitic parameters

and non-radiative recombination, which can predict and analyze the characteristics of DFB lasers [15]. Starting from the equivalent circuit model, shaping piecewise step current waveform [16] and continuously shaped injection current [6] based on rate equations are raised to suppress the ROs. The latter method overcomes the discontinuity of the former. Nevertheless, due to involves many areas of photonics, the determination of the shaping current parameters is the key to judging the shaping results, which is still a challenging inverse problem. The traditional numerical method presumes a set of parameters based on the parameter ranges to be inversed and compute the desired output waveform. Afterwards, the calculated waveform is contrasted with the target one and a set of parameters would be output when achieving the target precision or the maximum iteration. This method is limited by the iteration and has the characteristics of large randomness and slow speed. In the case of involving nonlinear processes, the traditional inverse design typically adopts the simulated annealing method [17], genetic algorithm [18], [19], gradient descent [20], etc. However, these approaches are also restricted by the iteration and usually need control equation when optimizing parameters.

Due to the flexibility and high performance of artificial neural networks (ANNs) [21], many research works have been recently carried out in fast inverse design based on optical models [22], [23], [24], [25]. Compared with ANN, convolutional neural network (CNN) is a special neural network that introduces convolution and pooling operations to generate deep features, thereby enhancing the discrimination and reducing the computational cost. CNN has been applied to signal extraction [26] and analysis [27] in photonics, which is faster and more accurate than traditional methods. The shaping current technique can be mapped by the trained CNN and further save the computing time of the control equation when realizing the parameter optimization.

In this paper, in order to accelerate the process of shaping current, an improved waveform based on rate equations and Fourier basic function of higher order is demonstrated. Initially, the characteristics of shaping current techniques are simulated, so as to get a group of training samples. Afterwards, a CNN model is trained to inversely approximate the characteristics of the technique to achieve the parameter optimization of shaping current inputs, while overcoming the computational cost problem in inverse design. In the combination of CNN and the DFB laser model, it can be seen from the output power that the ROs caused by the direct modulation are completely eliminated by injecting the shaping current waveforms. Moreover, to verify the proposed shaping current waveform, a time division multiplex passive optical network (TDM-PON) by adopting the DFB laser model as a directly modulated source is constructed. After long-distance bidirectional signal mode fiber (SMF) transmission, the Q-Factor and BER of the received signal still meet the communication conditions. The results illustrate that the shaping current with low cost and high reliability can work effectively for increasing the communication rate and bandwidth of TDM-PON. In this way, the performance of the DFB laser is guaranteed, but also the TDM-PON is optimized.

## II. Expression of High-Order Shaping Current for DFB Lasers

### A. Derivation of High-Order Shaping Current Formula

The rate equations describe the close relationship between the carrier density and photon density as shown in equations (1) and (2) [13].

$$\frac{dN}{dt} = \frac{J_0 + J(t)}{\alpha} - G(N(t), S(t))S(t) - \gamma_s N(t), \quad (1)$$

$$\frac{dS(t)}{dt} = -\gamma_c S(t) + \Gamma G(N(t), S(t)) S(t), \quad (2)$$

where $G(S(t), N(t))$ is the optical gain coefficient containing nonlinear effects, $J_0$ and $J(t)$ are the bias and modulation currents. $\alpha = eV_{act}$, and $e$ is a charge of an electron. $V_{act}$ is the volume of the active region which is expressed as $dWL$. $d$ is the active layer thickness. $W$ and $L$ are the width and length of the active area, respectively, and their values are defined as 1. $\Gamma$ is the field limiting factor, $\gamma_c$ and $\gamma_s$ are the attenuation rate of $N(t)$ and $S(t)$, respectively.

Without modulation ($J(t) = 0$), the nonlinear gain around the still operating point ($S_0$, $N_0$) is extended to the first order.

$$G(N, S) = G_0 + G_n(N - N_0) + G_p(S - S_0). \quad (3)$$

The stable state solution of the rate equations indicates the varying of the $N$ and $S$ along the injected current. In the case of $dS/dt = dN/dt = 0$, the ($S_0$, $N_0$) is substituted in (1) and (2).

$$G_0 S_0 = \frac{J_0}{ed} - \gamma_s N_0, \quad (4)$$

$$\Gamma G_0 = \gamma_c. \quad (5)$$

The current is defined as $J + J_m = (J_0 + J(t))/(\gamma_s N_0 ed)$-1. The dimensionless $S(t)$ and $N(t)$ are expressed as $s(\tau) = S(t)/S_0$ and $n(\tau) = N(t)/N_0 - 1$. $g = G/G_0$ is the dimensionless gain i.e.

$$g(n, s) = 1 + \frac{\gamma_n}{J\gamma_s} n - \frac{\gamma_p}{\gamma_c}(s - 1), \quad (6)$$

where $\gamma_n$ and $\gamma_p$ are the gain variations with the carrier and photon density respectively. $\omega_R = \sqrt{\gamma_c\gamma_n + \gamma_s\gamma_p}$ and $\tau = t\omega_R$ are the dimensionless angle frequency and time relative to the relaxation oscillation angle. The dimensionless rate equations are expressed as

$$\frac{dn}{d\tau} = \frac{\gamma_s}{\omega_R}(J + J_m - n - Jg(n, s)s), \quad (7)$$

$$\frac{ds}{d\tau} = \frac{\gamma_c s}{\omega_R}\left[g(n, s) - 1\right]. \quad (8)$$

The equation of expected $s(\tau)$ is assumed as $s(\tau) = e^{y(\tau)}$. The first-order differential equation for $s$ is

$$\frac{ds}{d\tau} = e^{y(\tau)} \cdot y'(\tau). \quad (9)$$

Combining equations (8) and (9), we can get the following equation

$$n(\tau) = \frac{J\gamma_s}{\gamma_n\gamma_c}\left[y'(\tau)\omega_R + \gamma_p(s - 1)\right]. \quad (10)$$

Combining (7) and (10), the injection current of the required waveform can be expressed as

$$J_m = \frac{J\omega_R^2}{\gamma_n \gamma_c}\left[y''(\tau) + \left(\frac{\gamma_p + \gamma_n}{\omega_R}s + \frac{\gamma_s}{\omega_R}\right)y'(\tau) + (s-1)\right]. \tag{11}$$

### B. Equivalent Circuit Modeling for DFB Laser

An equivalent circuit model of the DFB laser is developed based on the rate equations and simulates the dynamic characteristics. It is assumed that the carrier density and photon density in the cavity are uniform.

$$\frac{dN}{dt} = \frac{I_j}{\alpha} - R_n(N) - R_r(N) - GS, \tag{12}$$

$$\frac{dS}{dt} = \Gamma GS + \Gamma\beta R_r(N) - \frac{S}{\tau_p}, \tag{13}$$

where $N$ and $S$ represent carrier density and photon density. $I_j$ is a time-dependent injected current. $R_n(N)$ and $R_r(N)$ denote the rate of non-radiative and radiation recombination respectively. $G$ is optical gain. $\Gamma$ is the optical-confinement factor. $\beta$ represents the factor of spontaneous-emission. $\tau_p$ is the photon lifetime.

The first portion on the behind of the (12) indicates the ascension of $N$ resulting from $I_j$. The other parts indicate that the non-radiative recombination and radiative recombination of $S$ lead to the decay of $N$. The first and second parts behind (13) illustrate the increasing $S$ resulting from $G$ and the compound coupling of spontaneous emission to laser mode. The last section indicates the reduction of $S$ because of optical loss.

The $R_n(N)$ and $R_r(N)$ can be expressed as

$$R_n(N) = A_{n1}N + A_{n2}N^2 + A_{n3}N^3, \tag{14}$$

$$R_r(N) = A_{r1}N + A_{r2}N^2. \tag{15}$$

It is necessary to learn about the Shockley relationship [28] between $N$ and the junction voltage to establish the DFB laser model by using (12) and (13)

$$N = N_e\left[\exp\left(\frac{V_j}{\eta V_T}\right) - 1\right]. \tag{16}$$

Substituting (16) into (12).

$$I_j = C_d\frac{dV_j}{dt} + I_{st} + I_r + I_n, \tag{17}$$

where $C_d$ is the junction diffusion capacitance, $I_n$, $I_r$, and $I_{st}$ are the different recombination currents. They can be concretely expressed as $C_d = \alpha N_e \exp(V_j/\eta V_T)/\eta V_T$, $I_n = \alpha R_n(N)$, $I_r = \alpha R_r(N)$, and $I_{st} = \alpha GS$.

Multiplying $eV_{act}$ on both sides of (13) and it can be transformed to

$$I_{st} + \beta I_r = \frac{V_{ph}}{R_{ph}} + C_{ph}\frac{dV_{ph}}{dt}. \tag{18}$$

The equivalent circuit model of DFB laser is constructed from two standard circuit equations (17) and (18). The $V_{ph}$ obtained by these two equations is not an actual observable quantity, but it can be expressed as $V_{ph} = sV_{act}V_T$. There is also a certain relationship between the output power and $V_{ph}$, i.e.

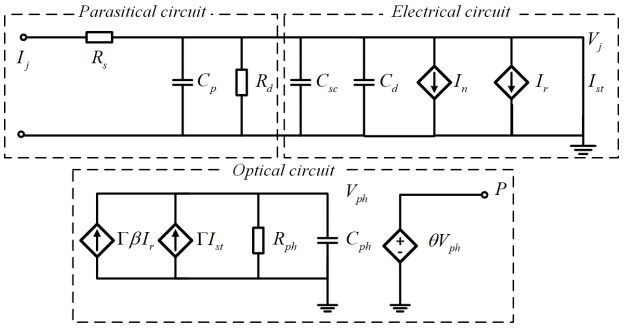


Fig. 1. Graph of DFB laser model which contains parasitical circuit, electrical circuit, and optical circuit.

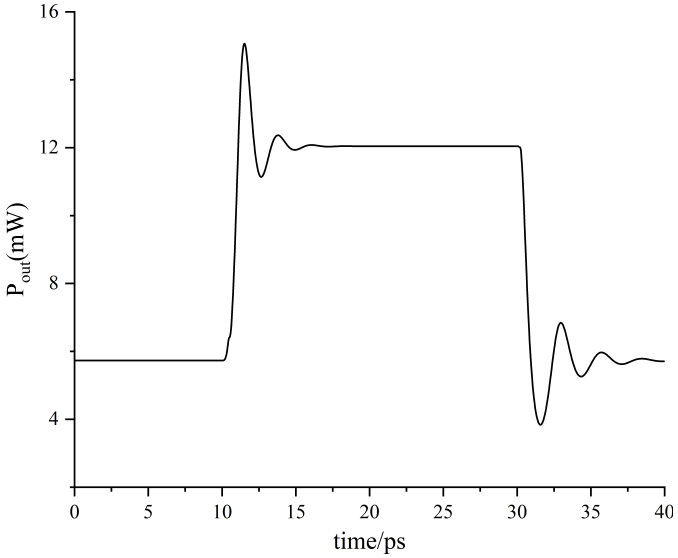


Fig. 2. Optical output power versus time from the DFB laser's equivalent circuit model.

$$P = \theta V_{ph}, \tag{19}$$

where $\theta$ is the angle of emergence.

Therefore, the correlation between $s$ and $P$ is stated as

$$P = \theta V_{act} V_T s. \tag{20}$$

The correlation between $J_m$ and the output power is expressed as

$$J_m = \frac{J\omega_R^2}{\gamma_n\gamma_c}\left[y''(\tau) + \left(\frac{\gamma_p + \gamma_n}{\omega_R}\frac{P}{\theta V_{act}V_T} + \frac{\gamma_s}{\omega_R}\right)y'(\tau) + \frac{P}{\theta V_{act}V_T} - 1\right]. \tag{21}$$

As shown in Fig. 1, the DFB laser equivalent circuit model consists of parasitic, electrical, and optical circuits, which considers the effect of parasitic parameters and non-radiative recombination. The equivalent circuit model is established based on rate equations, which can give the output power by injecting the current. The DFB laser is simulated and analyzed by PSpice and the simulation results can well simulate the output characteristics of the DFB laser. At present, the most prominent problem we face when using the direct modulation

TABLE I
PARAMETER VALUES FOR THE DFB LASER

| Symbol | Value | Description |
|---|---|---|
| $\Gamma$ | 0.25 | Mode-confinement factor |
| $V$ | $1.78\times10^{-11}cm^3$ | Active-layer volume |
| $\beta$ | $9.0\times10^{-5}$ | Spontaneous-emission factor |
| $\tau_p$ | $0.76ps$ | Photon lifetime |
| $A_{n1}$ | $1.0\times10^{8}s^{-1}$ | Deep-level-recombination coefficient |
| $A_{n2}$ | $1.1\times10^{-17}m^3s^{-1}$ | Low-level injection Auger-recombination coefficient |
| $A_{n3}$ | $2.0\times10^{-41}m^6s^{-1}$ | High-level injection Auger-recombination coefficient |
| $A_{r1}$ | $4.2\times10^{8}s^{-1}$ | Low-level injection radiative recombination coefficient |
| $A_{r2}$ | $1.5\times10^{-16}m^3s^{-1}$ | High-level injection radiative recombination coefficient |
| $\eta$ | 2 | Empirical constant |

Table I lists the parameters we use to establish the DFB laser model.

technique is that the output waveform will produce ROs. The output power in Fig. 2 can be obtained by injecting the ideal step current that the high level is 10 mA and the low level is -10 mA into the constructed DFB laser. The power contains ROs that are spike pulses with random changes in amplitude, pulse width, and interval. ROs appear at transient changes in current caused by resonance-like phenomena and limit the transmission rate of optical communication systems.

### C. Selection of Desired Waveforms

The photon density is expressed by $s(\tau) = e^{y(\tau)}$. The output waveform is selected in the form of approximating rectangular pulse, and we split it into two symmetric parts. To be specific, the output waveform will perform the $s_{up}$ and $s_{down}$. The high-order Fourier series approach is employed to restrict the expected waveform for easier realizing stable near-rectangular results. The basis function $y(\tau)$ is given by

$$y(\tau) = p(x) + \left[\sum_{k=1}^{N} b_k \sin(k\pi f(x))\right]^4, \tag{22}$$

where $x = \tau/T$. $T$ is the time period to complete the rising and falling edges. The f-function $f(x) = (a+1)x/(ax+1)$ is introduced to obtain shorter transition time in the process of rising and falling by fewer basis functions, where $a = 2$. There are several conditions that the p-function needs to satisfy in Table II.

At $x = 0$ and $x = 1$, the first, second, and third derivatives of the p-equation are 0 to ensure that the first derivative of $J_m$ is 0. Furthermore, a physically reasonable requirement is that the total shaping current $(3 + J + J_m \geq 0)$ into the laser must be nonnegative all the time.

On the basis of conditions in Table II, the rising and falling edges of the output waveform are restricted from different p-equations. Eq. (23) is substituted into $s(\tau) = e^{y(\tau)}$ to gain the desired waveform of the rising edge, while Eq. (24) is taken into $s(\tau) = e^{y(\tau)}$ that can get the desired waveform of the falling edge.

TABLE II
CONSTRAINTS OF P-EQUATION

| Symbol | Value |
|---|---|
| p(0) | $\ln[s(0)]$ |
| $p'(0)$ | 0 |
| $p''(0)$ | 0 |
| $p'''(0)$ | 0 |
| $p'(1)$ | 0 |
| $p''(1)$ | 0 |
| $p'''(1)$ | 0 |
| p($T$) | $\ln[s(T)]$ |

The functional forms of f-function and p-function refer to the literature [13]. The conditions that the equations need to satisfy are obtained through the literature [13] and repeated simulations.

TABLE III
PARAMETER VALUES FOR THE EQUATION

| Symbol | Value | Description |
|---|---|---|
| $J$ | 2/3 | bias current |
| $1/\omega_R$ | $45ps$ | frequency of relaxation oscillation |
| $\gamma_c$ | $3.6\times10^{11}s^{-1}$ | the attenuation rate of photon |
| $\gamma_n$ | $1.333\times10^{9}s^{-1}$ | gain variation with carrier density |
| $b_k$ | constant | constant |
| $\gamma_s$ | $1.458\times10^{9}s^{-1}$ | the decay rate of spontaneous carrier |
| $\gamma_p$ | $2.4\times10^{9}s^{-1}$ | gain variation with photon density |

Table III shows the values we employ which refer to Lucas' research [13].

TABLE IV
THE TRANSITION TIMES IN RISING AND FALLING EDGES

| | $N=3$ | $N=5$ | $N=8$ |
|---|---|---|---|
| up transition | 1.75 | 1.7 | 1.68 |
| down transition | 1.85 | 1.8 | 1.8 |

$$p(x) = (-20x^7+70x^6-84x^5+35x^4)\ln\frac{s(0)}{s(T_0)} + \ln[s(T_0)], \tag{23}$$

$$p(x) = (-20x^7+70x^6-84x^5+35x^4)\ln\frac{s(T_1)}{s(0)} + \ln[s(0)]. \tag{24}$$

Third-order continuous shaping current means that the order of the Fourier basis function is 3rd-order, when $N = 3$, $y(\tau) = p(x) + \left[\sum_{k=1}^{3} b_k \sin(k\pi f(x))\right]^4$. Here, $b_k$ ensures that the waveform $s(\tau) = e^{y(\tau)}$ is the desired output waveform and is a constant to be determined. Similarly, the same is true for the 5th and 8th-order continuous shaping current. Therefore, the determination of $b_k$ is paramount for the construction of shaping current waveforms. Table IV displays the transition times for the rising and falling edges in the different shaping currents. With the increasing order of Fourier series, the shaping current can be done more accurately and the shaping process in the rising and falling edges can be accelerated.

## III. PARAMETER SELECTION BASED ON CONVOLUTIONAL NEURAL NETWORK

The objective of training CNN is to produce the parameters $b_k$ and the total shaping current waveform according to the

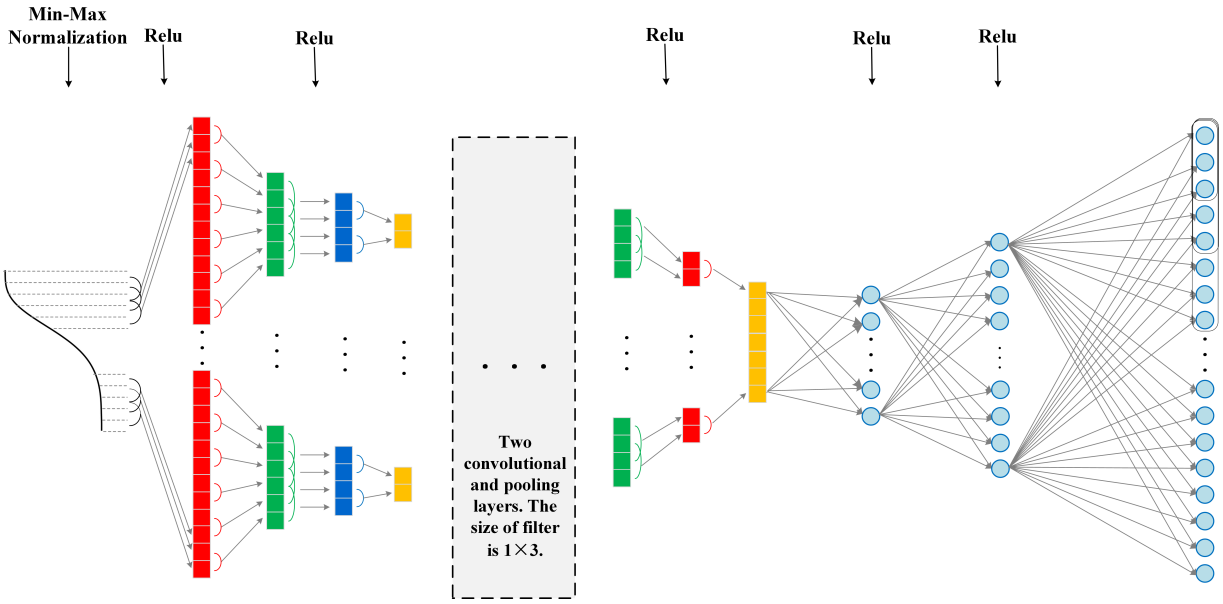


Fig. 3. Structure diagram of convolutional neural network.

desired output waveform. The 3rd, 5th, and 8th-order datasets are gathered by varying the parameter $b_k$, then calculating the total shaping current and desired output waveform. And these datasets are randomly split into training, validation, and test sets in the ratio of 0.85:0.05:0.1. In the 3rd-order data set, the parameter $b_k$ is randomly selected in the ranges of $b_1 = [0.1{:}0.3]$, $b_2 = [0.1{:}0.25]$, and $b_3 = [0.01{:}0.04]$. The parameter ranges for the 5th-order dataset are the same as previous five orders in the 8th-order. In the 8th order dataset, the ranges of parameter $b_k$ is $b_1 = [0.1{:}0.3]$, $b_2 = [0.1{:}0.2]$, $b_3 = [0.03{:}0.06]$, $b_4 = [0.01{:}0.03]$, $b_5 = [0.005{:}0.015]$, $b_6 = [0.005{:}0.015]$, $b_7 = [0.002{:}0.008]$, and $b_8 = [0.001{:}0.005]$.

### A. Architecture Design of Convolutional Neural Network

To obtain the neural network that can predict the properties of shaping current techniques with high accuracy, a CNN with data preprocessing, convolutional layers, pooling layers, and fully connected layers is constructed, as shown in Fig. 3.

The convolutional layer is responsible to scan the desired output waveforms (each waveform is sampled as 200 dots) for the presence or absence of particular features by the filter. According to the definition of convolution, it has two very important properties: local connection and weight sharing, which reduce the parameters of the convolutional layer and enhance the training efficiency. The size of the filter in the convolution layer is $1 \times 3$.

Generally, the pooling layer is optionally followed convolutional layer to decrease the number of features, so as to further reduce the number of training parameters and the overfitting degree. It also can maintain the invariance of scale and shift to a large extent. Although some information is obviously lost in this layer, CNN models are still successful.

Mean pooling and maximum pooling are two common pooling functions. Mean pooling is generally the average of the activity values of all neurons in the region [29].

$$y_{m,n}^{d} = \frac{1}{\left|R_{m,n}^{d}\right|} \sum_{i \in R_{m,n}^{d}} x_i. \tag{25}$$

Maximum pooling refers to selecting the maximum activity value of all neurons in a region as the representation in this region.

$$y_{m.n}^{d} = \max_{i \in R_{m,n}^{d}} x_i. \tag{26}$$

where $x_i$ is the activity value of each neuron in the region $R_k^d$. We adopt the maximum pooling, since it can reduce the deviation of the estimated mean caused by the parameter error of the convolutional layer compared with the average pooling. In this tutorial, the max-pooling layer follows each convolution layer. The stride is set on 1 and 2 for all the convolution and max-pooling layers respectively, and zero-padding is applied to them.

Three fully connected layers are put in the end to summarize the features extracted from the previous layers and output the final results. The previous two fully connected layers have 1024 and 2048 neurons respectively. The output layers have 203, 205, and 208 neurons respectively, when predicting the characteristics of 3rd, 5th, and 8th-order shaping current techniques. And the output layer is responsible for outputting shaping currents and parameters. The RELU (Rectified Linear Unit) activation function is adopted in the convolution and fully connected layers to alleviate the vanishing gradient problem and accelerate the convergence rate of gradient descent.

### B. The Evaluation of Convolutional Neural Network

The performance of CNN is evaluated by MSE (mean square error, i.e., the difference between the predicted values

TABLE V
THE MSES BETWEEN THE THEORETICAL AND PREDICTED PARAMETERS

(a) THE MSE OF THE 3RD-ORDER DATASET

| Parameter | $b_1$ | $b_2$ | $b_3$ |
|---|---|---|---|
| MSE | 1.44e-6 | 1.40e-6 | 1.88e-7 |

(b) THE MSE OF THE 5TH-ORDER DATASET

| Parameter | $b_1$ | $b_2$ | $b_3$ | $b_4$ | $b_5$ |
|---|---|---|---|---|---|
| MSE | 6.7e-6 | 2.11e-6 | 1.2e-6 | 3.99e-7 | 8.47e-8 |

(c) THE MSE OF THE 8TH-ORDER DATASET

| Parameter | $b_1$ | $b_2$ | $b_3$ | $b_4$ |
|---|---|---|---|---|
| MSE | 2.29e-6 | 1.12e-6 | 5.01e-7 | 2.97e-7 |
| Parameter | $b_5$ | $b_6$ | $b_7$ | $b_8$ |
| MSE | 2.82e-8 | 1.12e-7 | 3.91e-8 | 3.71e-7 |

of CNN and the theoretical ones), which can be defined as

$$MSE = \frac{\sum_{i=1}^{N} (y_i - y_i')^2}{N}, \tag{27}$$

where $y_i$ is the $i^{th}$ theoretical value, $y_i'$ is the $i^{th}$ predicted value. $N$ is the number of one batch, which is defined as 2, 048.

The closer the MSE is to 0, the closer the predicted value of the CNN is to the theoretical value. Fig. 4 illustrates the MSEs of the rising and falling edges for the training and validation sets on the 3rd, 5th, and 8th-order data sets. To clearly observe the value of MSE, only the value for the 5000 previous epochs is shown in Fig. 4. The final MSEs of the three training sets can converge to $10^{-3}$, $10^{-2}$, and $10^{-1}$ respectively, which means the predicted values of shaping current and parameters would be close to the theoretical ones.

## IV. PREDICT AND VERIFY THE PARAMETER OF SHAPING CURRENT WAVEFORM

Our shaping current waveform obtained from predicted parameters is demonstrated on the DFB laser model, whose results illustrate the suppression of ROs by the shaping current. The shaping current waveform and DFB model are simulated in TDM-PON. The performance of the system is also analyzed based on Q-factor and BER.

### *A. Parameter Selection of Shaping Current Waveform by CNN*

The CNN model is designed to address the problem of parameter selection in the continuous shaping current waveform. After training, the performance and accuracy of CNN are objectively verified by the MSEs of the test sets. To intuitively prove the ability of CNN in predicting the parameters of shaping current waveform, two hundred sets of samples are randomly selected from the test sets of 3rd, 5th, and 8th-order data sets (different from the training and validation datasets).

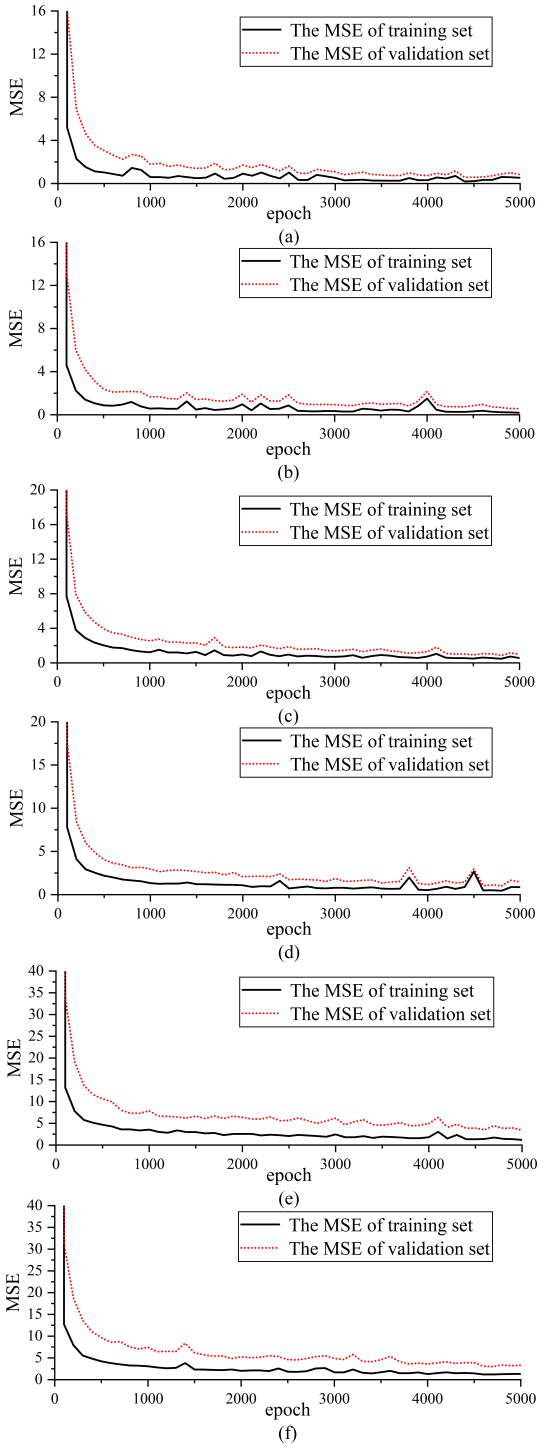


Fig. 4. Validation performance of the CNN models based on shaping current technique. (a) In the rising edge, the MSE of 3rd-order data between the theoretical and approximated values. (b) In the falling edge, the MSE of 3rd-order data between the theoretical and approximated values. (c) In the rising edge, the MSE of 5th-order data between the theoretical and approximated values. (d) In the falling edge, the MSE of 5th-order data between the theoretical and approximated values. (e) In the rising edge, the MSE of 8th-order data between the theoretical and approximated values. (f) In the falling edge, the MSE of 8th-order data between the theoretical and approximated values.

To verify the consistency of the predicted parameters by CNN and theoretical parameters, we calculate the MSE between them. As can be seen from Table V, the MSE is very

TABLE VI
THE COMPARISONS BETWEEN THE THEORETICAL AND PREDICTED PARAMETERS

(a) THE PARAMETERS COMPARISON OF THE 3RD-ORDER DATASET

| Parameters | $b_1$ | $b_2$ | $b_3$ |
|---|---|---|---|
| V1 | 0.164 | 0.115 | 0.0118 |
| V2 | 0.16556 | 0.11438 | 0.012171 |
| Error | 0.00156 | 0.00062 | 0.000371 |

(b) THE PARAMETERS COMPARISON OF THE 5TH-ORDER DATASET

| Parameters | $b_1$ | $b_2$ | $b_3$ | $b_4$ | $b_5$ |
|---|---|---|---|---|---|
| V1 | 0.1 | 0.196 | 0.06 | 0.016 | 0.007 |
| V2 | 0.10644 | 0.19347 | 0.06001 | 0.01697 | 0.00662 |
| Error | 0.00644 | 0.00253 | 0.00001 | 0.00097 | 0.0008 |

(c) THE PARAMETERS COMPARISON OF THE 8TH-ORDER DATASET

| Parameters | $b_1$ | $b_2$ | $b_3$ | $b_4$ |
|---|---|---|---|---|
| V1 | 0.22 | 0.1 | 0.057 | 0.01 |
| V2 | 0.2174 | 0.101 | 0.05603 | 0.01055 |
| Error | 0.0026 | 0.001 | 0.00097 | 0.00055 |
| Parameters | $b_5$ | $b_6$ | $b_7$ | $b_8$ |
| V1 | 0.008 | 0.005 | 0.0072 | 0.0014 |
| V2 | 0.00789 | 0.005032 | 0.007211 | 0.00139 |
| Error | 0.00011 | 0.000032 | 0.000011 | 0.00001 |

close to 0 which demonstrates the performance of CNN is significant.

To further determine the prediction performance of CNN, we randomly select a sample from the test set of 3rd, 5th, and 8th-order datasets respectively and inject them into CNN to obtain the corresponding parameters and shaping currents. Table VI lists the comparison between the predicted parameters of CNN and the theoretical values. V1 is the theoretical parameter, and V2 is the predicted value of CNN. Error is the absolute error between V1 and V2. As can be seen from Table VI, the absolute error between V1 and V2 is small, which indicates that the parameters predicted by CNN are precise.

The theoretical shaping current waveforms and the ones predicted by CNN which correspond to the parameters in Table VI are shown in Fig. 5. In these figures, each point represents the value of shaping current predicted by CNN, and the black line represents the theoretical one. Comparative results of the shaping current waveforms demonstrate that the predicted values can match well with the theoretical ones. It can be seen that CNN can achieve a high-precision capturing of the complete relationship among the parameters, the desired output waveform, and the injection current.

A set of 8th-order desired output waveform (different from train, validation, and test sets) is put into CNN to further illustrate the validity of CNN. The predicted values of parameters $b_k$ are [0.282147, 0.18342, 0.05874, 0.02106,_0.00559, 0.00552, 0.00484, 0.00135], and the calculated shaping current from these parameters is shown in Fig. 7.

### *B. Verify the Waveform by the Equivalent Circuit Model*

In order to illustrate the effectiveness of our proposed method, the unmodulated current and the shaping current waveform are put into the DFB laser model. Since the

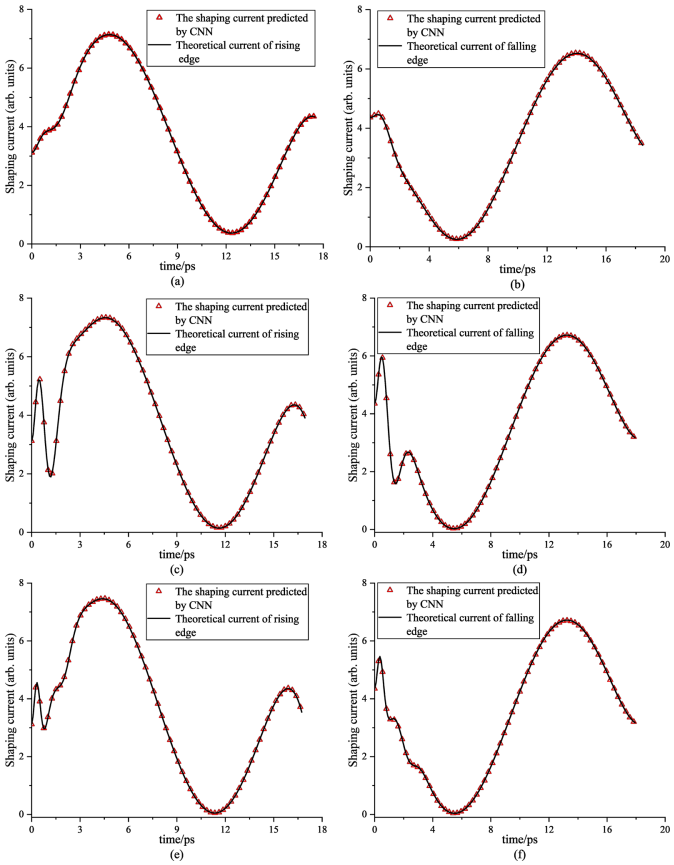


Fig. 5. The comparison of shaping current waveform between the theoretical and the obtained from CNN predicted parameters. (a), (c), and (e) In the rising edge, the 3rd, 5th, and 8th-order theoretical and approximated values. (b), (d), and (f) In the falling edge, the 3rd, 5th, and 8th-order theoretical and approximated values.

powerful ability of CNN to predict the parameters, the shaping currents of rising and falling edges are calculated based on the predicted parameters in Table VI and are integrated, as shown in Fig. 6 (a), (c), and (e). And then, the entire currents are injected into the DFB laser.

The output power in Fig. 2 resulting from the unmodulated current has obvious nonlinear distortion. The ROs are caused by the interaction between the optical field and carrier density, which will cause distortion in the output light pulse and degrade the quality of the optical spectrum in the output. Though the precarious state can eventually get stable, the transmitted information and communication performance will be interfered. By comparison, the black curves in Fig. 6. (b), (d), and (f) illustrate the output power obtained by injecting the continuous shaping current waveforms in Fig. 6 (a), (c), and (e) into the DFB laser model, and the ROs are almost suppressed. The shaping current can be used in communication system to enhance the performance when the constructed DFB laser is used as transmitter.

The shaping current calculated from [0.282147, 0.18342, 0.05874, 0.02106, 0.00559, 0.00552, 0.00484, 0.00135] is shown in Fig. 7 (a). The output power in Fig. 7(b) can be obtained by injecting the shaping current in Fig. 7(a) into the DFB laser, and it can be seen from the figure that the current can effectively suppress the ROs.

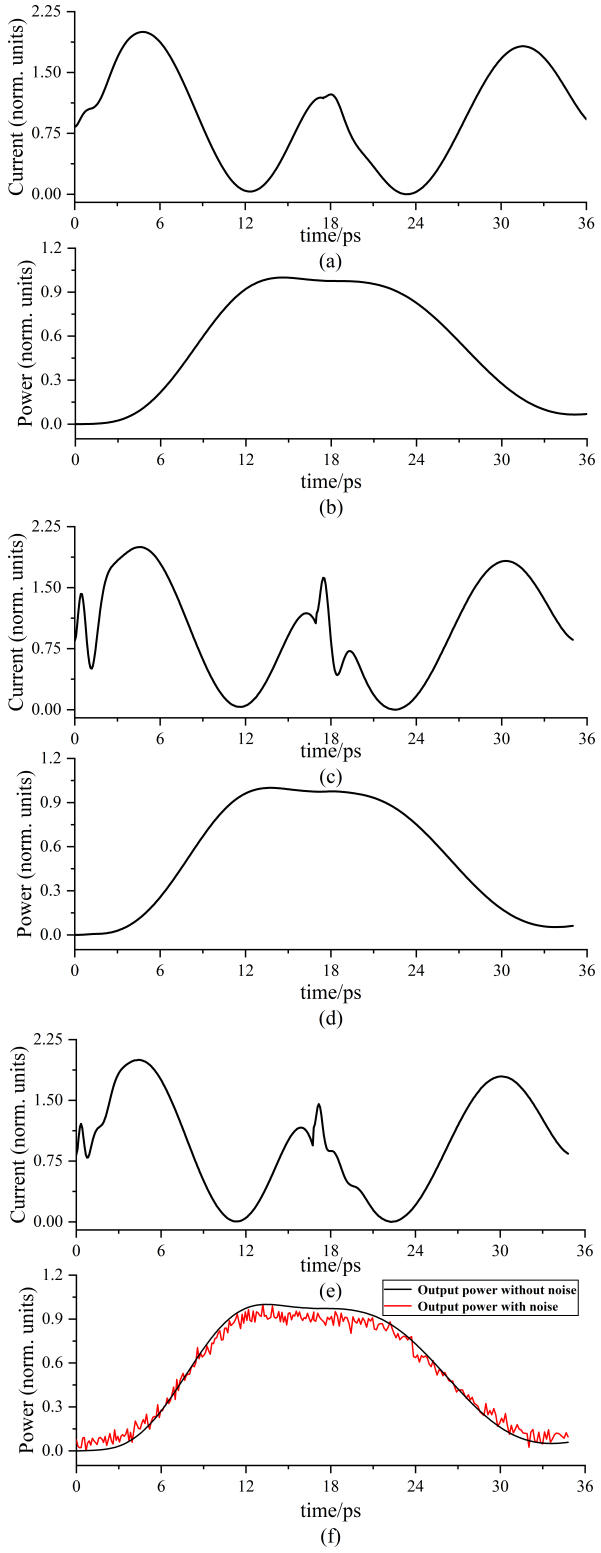


Fig. 6. The graph of the results under shaped currents. (a) The 3rd-order approximated shaping current. (b) The power resulted from the 3rd-order shaping current. (c) The 5th-order approximated shaping current. (d) The power resulted from the 5th-order shaping current. (e) The 8th-order approximated shaping current. (f) The power resulted from the 8th-order shaping current.

We can conclude that the proposed shaping current waveforms can perfectly suppress the ROs generated during the direct modulation of semiconductor lasers and further improve the modulation characteristics. The parameter selection by CNN can further promote the development of shaping current waveforms, and it has the advantages of simplicity, speed, and low consumption. Therefore, the method is significant for a laser to improve output efficiency.

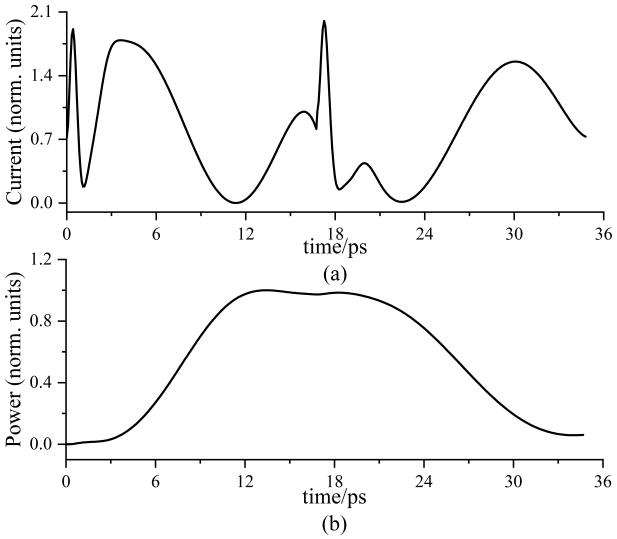


Fig. 7. The 8th-order shaping current and output power of DFB laser. (a) The shaping current is calculated from predicted parameters. (b) The output power by injecting current in (a) to DFB laser.

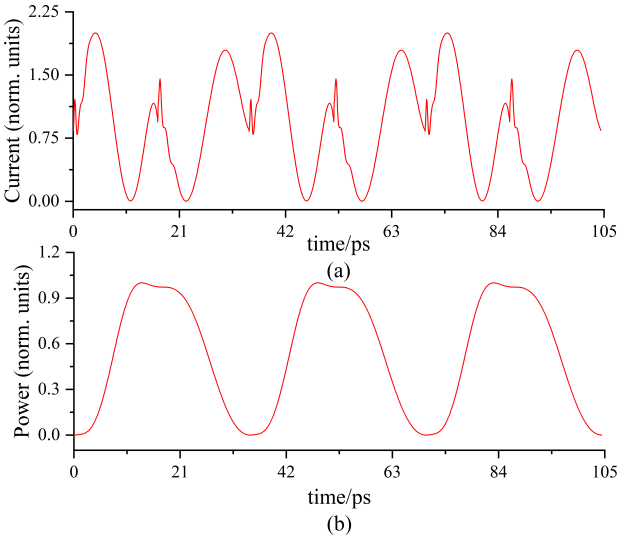


Fig. 8. Electrical and optical domain waveforms of the modulated signal. (a) The electrical domain waveform. (b) The optical domain waveform.

### *C. Application of the Shaping Current Waveform and the DFB Laser Model in TDM-PON*

The DFB laser model at 1,550 nm is used for an optical source at the downstream transmission of TDM-PON, and the whole simulation architecture is shown in Fig. 9. The data signal is the shaping current values obtained from predicted parameters by CNN, as shown in Fig. 6 (a), (c), and (e). Take 8th-order shaping current for example, the modulated signal in the previous three cycles of electrical and optical domain waveforms are shown in Fig. 8.

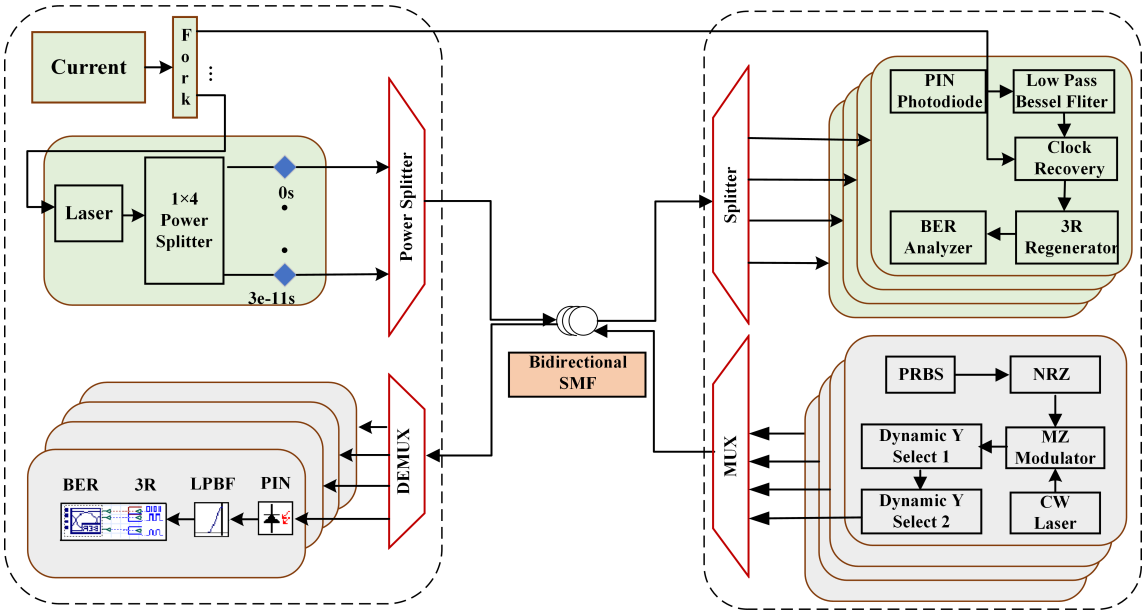


Fig. 9. Schematic diagram of TDM-PON system.

TABLE VII
TIME DELAY OF TDM NETWORK AT THE TRANSMISSION RATE OF 5GBPS

| parameter | | value | | | |
|---|---|---|---|---|---|
| Time Delay | Time slot | 0 | 1 | 2 | 3 |
| | Time delay(s) | 0 | $5\times10^{-11}$ | $2\times10^{-11}$ | $3\times10^{-11}$ |
| SMF | Wavelength(nm) | 1550 | | | |
| | Attention(dB/km) | 0.2 | | | |
| | Dispersion (ps/nm/km) | 16.75 | | | |
| | Dispersion slop (ps/nm$^2$/km) | 0.075 | | | |

To confirm the effectiveness of the proposed method, a step current waveform is injected into laser which is used as the light source for the communication system. Besides, the optical output power in Fig. 6 (f) is added 10% Gaussian noise to reproduce the influence of laser's noise and serves as the input power in the downstream link to verify the system performance. Four channels from the DFB laser model source are followed by a certain time delay (as shown in Table VII) to transmit the information in a specific time slot and then fed into a $1 \times 4$ power combiner.

After 10-80 km transmission in the bidirectional SMF, the signal is detected by four pin detectors via a $4 \times 1$ fork. Then the optical signals are converted into electrical signals. The target signals are filtered with noise immunity via low-pass Bessel filters. To recover the timing information from a data stream of high-speed serial link, the clock recovery components are connected to the transmitter and receiver section, respectively. Moreover, the recovered signals are transmitted to the BER analyzer for analysis. For upstream transmission, the continuous wave (CW) lasers are used for optical sources.

To distinguish the downstream and upstream channels, an optical delay of 1 is adopted in upstream transmission. For verifying the effectiveness of the DFB laser model and the shaping current waveforms, we only analyze the results

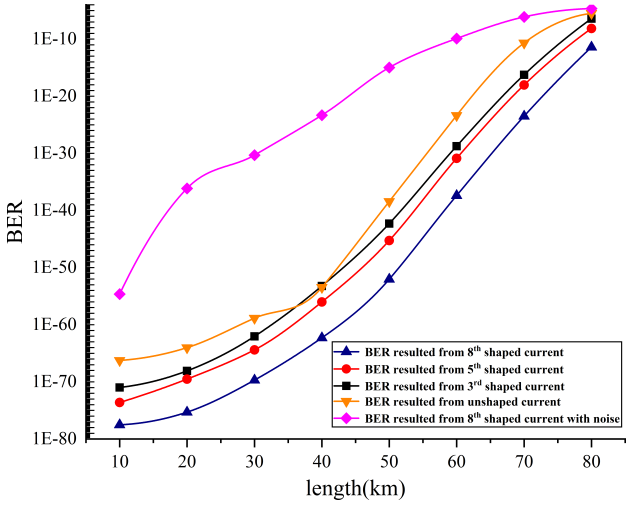


Fig. 10. Transmission distances versus BER for the downstream link.

of the downstream channel. At the data rate of 5Gbps, the amplitude modulation is used in the downstream transmission and the light source in the link is direct modulation DFB laser. In the downlink, the $-3$dB bandwidth of laser is about 12GHz, and the bandwidth of PIN photodiode is set to 12GHz. The Q-factor and minimum BER values of the received signals are analyzed to evaluate the performance of the system. To ensure the quality of the received signal, the Q-factor should be greater than 6 and the BER should be smaller than $10^{-9}$. The results of received Q-Factors from the BER analyzer can be seen in Fig. 11. Obviously, increasing the length of SMF reduces the Q-Factor.

The BER values under the different light source signals are shown in Fig. 10. When the power with noise serves as the input power of the downstream link, the BER value is bigger than the optical power (which is generated from different shaping current) without noise act as the input power, but the

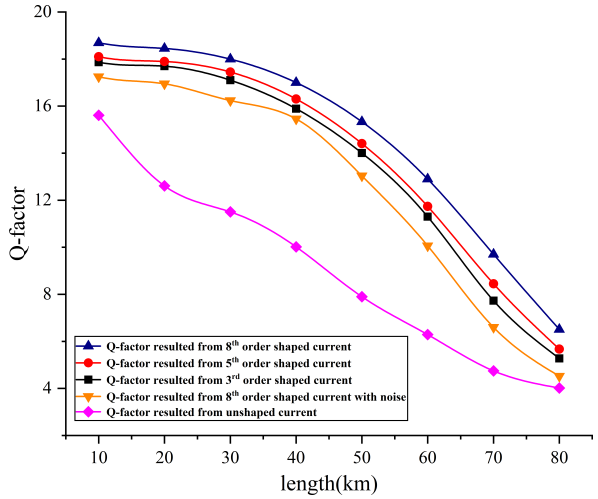


Fig. 11. Transmission distances versus Q factor for the downstream link.

BER value is still smaller than injecting the step current into the laser.

As can be seen from Fig. 11, the Q factor increases continuously with the increasing order of the shaping current. When the optical output power with noise serves as the input power of downstream link, the Q factor is lower than the optical power (which resulted from different shaping current) without noise acts as the input power and it is bigger than injecting step current to the laser. Such behavior is expected since suppressing ROs in the laser output power can improve the system performance, while adding noise to the power can reduce the system performance. Meanwhile, increasing the order of the shaping current can accelerate the shaping process and further improve the system performance.

The selection of the parameters for this study are several parameters in the shaping current waveform that have the paramount influence on suppressing the DFB laser ROs. Furthermore, we accelerate the shaping process to reach the ideal current which can increase the performance of the TDM-PON.

## V. Conclusion

In this tutorial, a novel shaping current waveform based on rate equations for suppressing the ROs of DFB lasers is proposed. The trained CNN is successfully applied to the complicated parameter optimization of 3rd, 5th, and 8th-order shaping current techniques. With the normalization of the input data, the proposed CNN works well in predicting the parameters. The analysis of parameters and shaping current predicted from CNN model shows that the trained model provides powerful computing ability in inversely simulating the shaping current technique behavior. Compared with injecting step current, the injection of shaping current waveforms obtained from CNN predicted parameters into the constructed DFB laser model can effectively suppress ROs in the output optical power. A TDM-PON utilizing the DFB laser model as the directly-modulated source is designed. The results demonstrate that the shaping current with low cost and high reliability can work powerfully for long-reach TDM-PON transmission system. Importantly, the performance of the DFB laser model and TDM-PON can be improved by increasing the order of shaping current, which can be very promising for the DFB laser and optical communication system.

The proposed technique has been applied in the simulation system. Potentially future study is considering the noise in the rate equations and applying the proposed method in the practical communication system.

## References

[1] L. M. Zhang, S. F. Yu, M. C. Nowell, D. D. Marcenac, J. E. Carroll, and R. G. S. Plumb, "Dynamic analysis of radiation and side-mode suppression in a second-order DFB laser using time-domain large-signal traveling wave model," *IEEE J. Quantum Electron.*, vol. 30, no. 6, pp. 1389–1395, Jun. 1994.

[2] J. Yu et al., "Applications of 40-Gb/s chirp-managed laser in access and metro networks," *J. Lightw. Technol.*, vol. 27, no. 3, pp. 253–265, Feb. 1, 2009.

[3] J. L. Wei, C. Sánchez, E. Hugues-Salas, P. S. Spencer, and J. M. Tang, "Wavelength-offset filtering in optical OFDM IMDD systems using directly modulated DFB lasers," *J. Lightw. Technol.*, vol. 29, no. 18, pp. 2861–2870, Sep. 15, 2011.

[4] M. M. H. Adib et al., "Colorless coherent TDM-PON based on a frequency-comb laser," *J. Lightw. Technol.*, vol. 40, no. 13, pp. 4287–4299, Jul. 1, 2022.

[5] Y. Zhang et al., "Study on two-section DFB lasers and laser arrays based on the reconstruction equivalent chirp technique and their application in radio-over-fiber systems," *IEEE J. Sel. Topics Quantum Electron.*, vol. 21, no. 6, pp. 232–240, Nov. 2015.

[6] Q. Ding et al., "Continuous current-injected waveforms shaping for suppressing relaxation oscillations of direct modulation based on equivalent circuit model," *Opt. Exp.*, vol. 30, no. 11, pp. 19273–19287, 2022.

[7] S. Sulikhah, S. L. Lee, and H. W. Tsao, "Improvement on direct modulation responses and stability by partially corrugated gratings based DFB lasers with passive feedback," *IEEE Photon. J.*, vol. 13, no. 1, pp. 1–14, Feb. 2021.

[8] K. Sato, S. Kuwahara, and Y. Miyamoto, "Chirp characteristics of 40-Gb/s directly modulated distributed-feedback laser diodes," *J. Lightw. Technol.*, vol. 23, no. 11, pp. 3790–3797, Nov. 2005.

[9] J. Yin, X. Xiao, and C. Yang, "Dynamics and suppression of relaxation oscillation caused by stimulated Brillouin scattering in optical fiber," in *Proc. 14th OptoElectron. Commun. Conf.*, Jul. 2009, pp. 1–2.

[10] R. Lang and K. Kobayashi, "Suppression of the relaxation oscillation in the modulated output of semiconductor lasers," *IEEE J. Quantum Electron.*, vol. QE-12, no. 3, pp. 194–199, Mar. 1976.

[11] Y. Suematsu and T.-H. Hong, "Suppression of relaxation oscillation in light output of injection lasers by electrical resonance circuit," *IEEE J. Quantum Electron.*, vol. QE-13, no. 9, pp. 756–762, Sep. 1977.

[12] L. Bickers and L. Westbrook, "Reduction of transient laser chirp in 1.5 $\mu$m DFB lasers by shaping the modulation pulse," *IEE Proc. J.*, vol. 133, no. 2, pp. 155–162, 1986.

[13] L. Illing and M. B. Kennel, "Shaping current waveforms for direct modulation of semiconductor lasers," *IEEE J. Quantum Electron.*, vol. 40, no. 5, pp. 445–452, May 2004.

[14] H. N. Nhat, D. T. T. Thuy, and N. A. Duc, "Analytical solution of the rate equation in direct modulation of semiconductor laser," in *Proc. Int. Conf. Adv. Technol. Commun.*, Oct. 2008, pp. 371–375.

[15] B. Nie et al., "Circuit model for the effect of nonradiative recombination in a high-speed distributed-feedback laser," *Current Opt. Photon.*, vol. 4, no. 5, pp. 434–440, 2020.

[16] B. Nie, Q.-A. Ding, C. Liu, X. Cheng, X. Wang, and L. Zhang, "Suppression of relaxation oscillations in DFB lasers through shaping injection current waveforms," in *Proc. IEEE 20th Int. Conf. Commun. Technol. (ICCT)*, Oct. 2020, pp. 975–979.

[17] S. Zommer, E. Ribak, S. Lipson, and J. Adler, "Simulated annealing in ocular adaptive optics," *Opt. Lett.*, vol. 31, no. 7, pp. 939–941, 2006.

[18] P.-H. Fu, T.-Y. Huang, K.-W. Fan, and D.-W. Huang, "Optimization for ultrabroadband polarization beam splitters using a genetic algorithm," *IEEE Photon. J.*, vol. 11, no. 1, pp. 1–11, Feb. 2019.

[19] S. Shu, "Evolving ultrafast laser information by a learning genetic algorithm combined with a knowledge base," *IEEE Photon. Technol. Lett.*, vol. 18, no. 2, pp. 379–381, Jan. 15, 2006.
[20] N. A. Ahmad, "A globally convergent stochastic pairwise conjugate gradient-based algorithm for adaptive filtering," *IEEE Signal Process. Lett.*, vol. 15, pp. 914–917, 2008.
[21] F. V. Celebi, "A different approach to gain computation in laser diodes with respect to different number of quantum-wells," *Optik, Int. J. Light*, vol. 116, no. 8, pp. 375–378, Aug. 2005.
[22] P. Feng and Y. Li, "Semiconductor laser parameter inverse design method based on artificial neural network and particle swarm optimization," *Chin. J. Lasers*, vol. 46, no. 7, 2019, Art. no. 0701001.
[23] Z. Ma and Y. Li, "Parameter extraction and inverse design of semiconductor lasers based on the deep learning and particle swarm optimization method," *Opt. Exp.*, vol. 28, no. 15, pp. 21971–21981, 2020.
[24] D. Liu, Y. Tan, E. Khoram, and Z. Yu, "Training deep neural networks for the inverse design of nanophotonic structures," *ACS Photon.*, vol. 5, no. 4, pp. 1365–1369, Apr. 2018.
[25] J.-S. Li and Z.-W. Bao, "Artificial neural network for the noise characteristics of laser modeling," in *Proc. Int. Conf. Mach. Learn. Cybern.*, vol. 5, 2004, pp. 3219–3222.
[26] C. Liu, L. Li, X. Huang, X. Wang, and C. Wang, "Audio signal extraction and enhancement based on CNN from laser speckles," *IEEE Photon. J.*, vol. 14, no. 1, pp. 1–5, Feb. 2022.
[27] S. Guo et al., "Automatic quantification of subsurface defects by analyzing laser ultrasonic signals using convolutional neural networks and wavelet transform," *IEEE Trans. Ultrason., Ferroelectr., Freq. Control*, vol. 68, no. 10, pp. 3216–3225, Oct. 2021.
[28] R. Tucker and D. Pope, "Circuit modeling of the effect of diffusion on damping in a narrow-stripe semiconductor laser," *IEEE J. Quantum Electron.*, vol. QE-19, no. 7, pp. 1179–1183, Jul. 1983.
[29] Q. Xipeng, *Neural Networks and Deep Learning*. Shanghai, China: China Machine Press, 2020.

**Qing-An Ding** received the M.S. degree in physics and electronics from the Nanjing University of Science and Technology, in 2004, and the Ph.D. degree in radio physics from Shandong University, China, in 2015. He is currently an Associate Professor with the School of Electronics and Information Engineering, Shandong University of Science and Technology, Qingdao, China. His research interests include computational electromagnetics, fiber-optic communications, and numerical methods for silicon photonics.

**Huixin-Liu** was born in Shandong, China. She received the bachelor's degree in electronic information science and technology from Qingdao Agricultural University in 2020. She is currently pursuing the master's degree in electronic and information with the Shandong University of Science and Technology. She is also engaged in artificial neural network.

**Xudong Cheng** was born in Jiangxi, China. He received the B.S. degree in communication engineering from the Shandong University of Science and Technology in 2020, where he is currently pursuing the M.S. degree majoring in circuits and systems with the College of Electronics and Information Engineering. He is also engaged in research on the parameter optimization of equivalent circuit model for high-speed DFB lasers. His research interests include parameter optimization of the equivalent circuit model of semiconductor lasers and simulation of the equivalent circuit model of semiconductor lasers.

**Xiao-Juan Wang** was born in Shandong, China. She received the bachelor's degree in electronic information engineering from Dezhou University in 2015. She is currently pursuing the master's degree in communication and information systems with the Shandong University of Science and Technology. Her research interests include parameter optimization of the equivalent circuit model of semiconductor lasers and simulation of the equivalent circuit model of semiconductor lasers. Her current research direction is parameter optimization of semiconductor lasers.

**Weiping Huang** (Senior Member, IEEE) received the Ph.D. degree in electrical engineering with major in photonics from the Massachusetts Institute of Technology (MIT), Cambridge, in 1989. He is currently the Dean and a Professor with the School of Information Science and Engineering, Shandong University, Qingdao, Shandong, China. He is internationally known for his contributions and expertise for photonic devices and integrated circuits, especially in the computer-aided design technologies for photonic devices and ICs. He has authored and coauthored more than 140 journal articles and 70 conference papers and holds seven U.S. patents. He is a member of OSA and the MIT Electromagnetics Academy. He was elected as a Cheung Kong Scholar by the Ministry of Education, China, and Li Ka Shing Foundation, Hong Kong, in 2000.

**Liuge Du** was born in Shandong, China. He received the B.S. and Ph.D. degrees in physics and optics from Shandong University, Qingdao, China, in 2007 and 2011, respectively. Currently, he is an Associate Researcher with the School of Information Science and Engineering, Shandong University. He is also engaged in research on modeling and design of silicon photonics and electromagnetics. His research interests include theory and method of computational electromagnetics and simulation of semiconductor devices.

**Gaoyang Zhu** (Member, IEEE) was born in Liaocheng, China. She received the Ph.D. degree in electronic science and technology from the School of Information Science and Engineering, Shandong University, Qingdao, China, in 2020. She is currently a Lecturer with the School of Electronics and Information Engineering, Shandong University of Science and Technology, Qingdao. Her current research interests include neural networks, computational electromagnetics, inversion of induction logging, and geophysical well-logging applications.

**Li Zheng** was born in Shandong, China. She received the Engineering degree from Liaocheng University in 2016, majoring in communication engineering, and the degree from the Shandong University of Science and Technology, majoring in information and communication engineering. She is currently engaged in microwave and optical communication research.

**Qunying Yang** received the bachelor's degree from the Department of Communication Engineering, Shandong University of Science and Technology in 2021, where she is currently pursuing the degree under supervision of Dr. Qing-An Ding. Her research interest is convolutional neural networks.